J Physiol 599.6 (2021) pp 1815–1831

The Journal of Physiology

Muscle myosin performance measured with a synthetic nanomachine reveals a class-specific Ca^{2+}-sensitivity of the frog myosin II isoform

Irene Pertici[1], Giulio Bianchi[1], Lorenzo Bongini[1], Dan Cojoc[2], Manuel H. Taft[3], Dietmar J. Manstein[3], Vincenzo Lombardi[1] and Pasquale Bianco[1]

[1] *PhysioLab, University of Florence, Sesto Fiorentino, FI, Italy*
[2] *IOM-CNR, Trieste, Italy*
[3] *Institute for Biophysical Chemistry, Fritz-Hartmann-Centre for Medical Research, Medizinische Hochschule Hannover, Hannover, Germany*

Edited by: Michael Hogan & Jolanda Van der Velden

Key points

- A nanomachine made of an ensemble of seven heavy-meromyosin (HMM) fragments of muscle myosin interacting with an actin filament is able to mimic the half-sarcomere generating steady force and constant-velocity shortening.
- To preserve Ca^{2+} as a free parameter, the Ca^{2+}-insensitive gelsolin fragment TL40 is used to attach the correctly oriented actin filament to the laser-trapped bead acting as a force transducer.
- The new method reveals that the performance of the nanomachine powered by myosin from frog hind-limb muscles depends on $[Ca^{2+}]$, an effect mediated by a Ca^{2+}-binding site in the regulatory light chain of HMM. The Ca^{2+}-sensitivity is class-specific because the performance of the nanomachine powered by mammalian skeletal muscle myosin is Ca^{2+} independent.
- A model simulation is able to interface the nanomachine performance with that of the muscle of origin and provides a molecular explanation of the functional diversity of muscles with different orthologue isoforms of myosin.

Abstract An ensemble of seven heavy-meromyosin (HMM) fragments of myosin-II purified from the hindlimb muscles of the frog (*Rana esculenta*) is used to drive a synthetic nanomachine that pulls an actin filament in the absence of confounding effects of other sarcomeric proteins. In the present version of the nanomachine the +end of the actin filament is attached to the laser trapped bead via the Ca^{2+}-insensitive gelsolin fragment TL40, making $[Ca^{2+}]$ a free parameter. Frog myosin performance in 2 mM ATP is affected by Ca^{2+}: in 0.1 mm Ca^{2+}, the isometric steady force (F_0, 15.25 pN) is increased by 50% ($P = 0.004$) with respect to that in Ca^{2+}-free solution, the maximum shortening velocity (V_0, 4.6 μm s^{-1}) is reduced by 27% ($P = 0.46$) and the maximum power (P_{max}, 7.6 aW) is increased by 21% ($P = 0.17$). V_0 reduction is not significant for the paucity of data at low force, although it is solidified by a similar decrease (33%, $P < 0.0001$) in the velocity of actin sliding as indicated by an *in vitro* motility assay (V_f). The rate of ATP-hydrolysis in solution (φ) exhibits a similar calcium dependence. Ca^{2+} titration curves for V_f and φ give K_d values of ~30 μM. All the above mechanical and kinetic parameters are independent of Ca^{2+} when HMM from rabbit psoas

Irene Pertici received her PhD in Molecular Medicine in 2018 under the supervision of Vincenzo Lombardi at the Physio-Lab, University of Florence. Her PhD project was devoted to the realization of a synthetic myosin-based nanomachine able to mimic the generation of a steady force and the shortening of striated muscle. The present study, framed within a multiscale *in vitro*, *in situ* investigation aimed at defining the mechanisms of function-dysfunction of striated muscle at different hierarchical levels, was partly realized during her stay at the Institute for Biophysical Chemistry at the Hannover Medical School. She is currently a postdoctoral researcher at the University of Florence.

DOI: 10.1113/JP280976

myosin is used, indicating that the Ca^{2+}-sensitivity is a class-specific property of muscle myosin. A unique multiscale model allows interfacing of the nanomachine performance to that of the muscle of origin and identifies the kinetic steps responsible for the Ca^{2+}-sensitivity of frog myosin.

(Received 16 October 2020; accepted after revision 25 January 2021; first published online 28 January 2021)
Corresponding author V. Lombardi: PhysioLab, University of Florence, Sesto Fiorentino (FI), 50019 Italy. Email: vincenzo.lombardi@unifi.it

Introduction

Contraction of striated (cardiac and skeletal) muscle is a result of the molecular motor myosin II arranged in two anti-parallel arrays in each sarcomere. Upon muscle activation the myosin motors, extending from the thick filaments at the centre of the sarcomere, attach to the nearby thin, actin-containing, filaments and pull them toward the sarcomere centre by an ATP-driven working stroke in the myosin globular domain (Huxley & Simmons, 1971; Rayment *et al*. 1993). The collective motor emerging from the mechanical coupling between myosin motors via their attachment to the thick filament backbone allows for the generation of steady force and shortening, recovering the processivity missed by muscle myosin II working as a single molecule for its short actin-attachment time during the ATP hydrolysis cycle (Lymn & Taylor, 1971; Uyeda *et al*. 1990). Cell studies have shown that the half-sarcomere is able to efficiently work across a wide range of externally applied loads and shortening velocities by tuning the number of heads attached to actin in proportion to the global filament load (Piazzesi *et al*. 2007). The underlying mechanism is the strain dependence of the chemo-mechanical steps of the ATPase cycle in the attached motors (Huxley, 1957; Huxley & Simmons, 1971; Dantzig *et al*. 1991), which ensures accelerated detachment when the attached motors become negatively strained, preserving the efficiency of the actin–myosin interaction. Cell studies, on the other hand, are complicated by the large ensemble of motor proteins and filaments, as well as by the confounding contribution of the other sarcomeric regulatory and cyto-skeleton proteins. *In vitro* single-molecule mechanics use purified proteins, allowing the definition of motor protein action in the absence of the effects of the other sarcomeric proteins. Single-molecule mechanics, however, cannot define the properties that uniquely emerge from the collective motor within the architecture of the half-sarcomere, such as the generation of steady power tuned to the external load and the possibility of selectively testing the regulatory mechanisms of the other sarcomeric proteins by integrating them in the system one at a time. These limits are overcome with the realization of a one-dimensional nanomachine titrated to contain the minimum number of motor molecules able to generate steady force and constant-velocity shortening upon interaction with an actin filament (Pertici *et al*. 2018). In the nanomachine, an ensemble of heavy-meromyosin (HMM) fragments from myosin II, carried on a piezo-nanomanipulator acting as a length transducer, interacts with an actin filament attached, with the correct polarity, to a bead trapped on the focus of a dual laser optical tweezers (DLOT) acting as a force transducer.

Here, we determine the performance of the nanomachine assembled using HMM fragments from the hindlimb muscles of the frog. The choice to power the nanomachine with myosin from frog skeletal muscle is justified by considering that the most reliable reference values available in the literature for the mechanical, kinetic and energetic parameters of muscle contraction come from muscles and intact single fibres of the frog (Hill, 1938; Huxley & Simmons, 1971; Ford *et al*. 1977; Linari & Woledge, 1995; Piazzesi & Lombardi, 1995). Thus, even if purifying myosin motors from frog muscle is quite challenging because of the fragility of the molecule at room temperature (Ferenczi *et al*. 1978; Elangovan *et al*. 2012), this myosin isoform represents the ideal system for interfacing the performance of the synthetic nanomachine to that of the muscle of origin and implementing model simulations that are able to provide an integrate multiscale view of the mechanics and energetics of muscle contraction.

In the original version of the nanomachine gelsolin, a Ca^{2+}-regulated actin-binding protein, was used to obtain correctly oriented bead-attached actin filaments [bead-tailed-actin (BTA)] (Suzuki *et al*. 1996). Here, we exploit a recent implementation of the BTA preparation (Pertici *et al*. 2020), which uses the Ca^{2+}-insensitive gelsolin fragment TL40 (Hypermol, Bielefeld, Germany; see Methods). The method, which has been demonstrated to fully preserve the performance of the nanomachine powered by HMM from fast mammalian muscle (Pertici *et al*. 2020), makes $[Ca^{2+}]$ a free parameter, opening the possibility of applying the nanomachine to investigations of any Ca^{2+}-regulated mechanism; the most important of these, but not the only one, is Ca^{2+}-dependent thin filament activation by the regulatory proteins troponin and tropomyosin.

We find that the performance of the basic version of the nanomachine, made by an ensemble of frog myosin HMM interacting with an actin filament, is sensitive to Ca^{2+}:

the isometric steady force (F_0) and the maximum power (P_{max}) increase in the presence of Ca^{2+} 0.1 mM (+50% and +21% respectively), whereas the maximum shortening velocity (V_0) reduces (−27%). Given the reduction of the duty ratio at low load, the probability of maintaining continuous interaction between the actin filament and the motor ensemble becomes progressively lower toward the velocity axis. Consequently, the number of force-velocity (F–V) points in this region is low and the error in the estimate of V_0 high, so that the Ca^{2+}-dependent reduction in V_0 is not significant. However, a significant depressant effect of Ca^{2+}, similar to that of V_0, is found for the velocity of actin sliding in an *in vitro* motility assay (IVMA) (V_f), as well as for the rate of ATP-hydrolysis (φ). None of the above mechanical and kinetic parameters of HMM fragments of myosin from fast mammalian skeletal muscle is affected by Ca^{2+}, indicating that the Ca^{2+}-sensitivity of skeletal muscle myosin of vertebrates comprises a class-specific property that is lost in mammals. The nanomachine performance (F–V relationship, maximum power and underlying energetics) is interfaced to the corresponding muscle using a model simulation with a unique kinetic scheme (Pertici *et al*. 2018; Pertici *et al*. 2020), demonstrating the ability of the nanomachine to recapitulate the emergent properties of the muscle of origin and identify the myosin-based functional diversity of muscles of different classes of animals. The effect of Ca^{2+} on the performance of the frog myosin-based nanomachine is explained by the model with a Ca^{2+}-dependent reduction in the strain sensitivity of the rate of motor detachment at the end of the stroke.

Methods

The preparation of proteins and the mechanical experiments were performed in the PhysioLab, University of Florence [Sesto Fiorentino (FI), Italy]. Solution kinetic measurements were performed at the Institute for Biophysical Chemistry, Medizinische Hochschule Hannover (Hanover, Germany).

Ethical approval

Frogs (*Rana esculenta*), housed in a humid environment at 4–6°C for no longer than 2 months, were killed by decapitation and destruction of the brain and the spinal cord at 4°C, in accordance with the Italian regulation on animal experimentation (Authorization 956/2015-PR) and in compliance with Decreto Legislativo 26/2014 and EU directive 2010/63. In total, 10 male frogs weighing 30–40 g (aged 2 years), supplied by the registered company *Fish and Frog* (Ravenna, Italy), were used for the experiments. Adult male New Zealand White rabbit, provided by Envigo (Casatenovo, Italy), were housed at CeSAL, University of Florence, under controlled conditions of temperature (20 ± 1°C) and humidity (55% ± 10%) and were killed by injection of an overdose of sodium pentobarbitone (150 mg kg^{-1}) in the marginal ear vein, in accordance with Italian and European regulation as oulined above. Two rabbits were used for the experiments.

Preparation of proteins

Frog myosin was purified from frog hindlimb muscle tissue according to well established protocols aimed at preserving the quality of myosin (Elangovan *et al*. 2012). HMM and S1 fragments were obtained by chymotryptic digestion of myosin (Ferenczi *et al*. 1978, Weeds & Taylor, 1975): a final concentration of 0.2 mg mL^{-1} α-chymotrypsin was added to the digestion solution [750 mM KCl, 10 mM Kpi, pH 6.5, 2 mM dithiothreitol (DTT) and EDTA-free anti-protease cocktail] containing either 2.5 mM $MgCl_2$ or 1 mM EDTA for HMM or S1 preparation, respectively. The reaction was stopped with 2 mM phenylmethylsulphonyl fluoride after 3 h (for HMM) or 2 h (for S1). The presence of 1 mM EDTA in the digestion mixture ensures the selective production of S1 over HMM. On SDS-PAGE gel, S1 obtained by chymotryptic digestion shows that the regulatory light chain (RLC) is absent (Weeds & Taylor, 1975). Undigested myosin and insoluble myosin fragments were precipitated by dialysing the digestion mixture overnight in cold room against a dialysis buffer (30 mM KCl, 20 mM Mops, pH 7.0, 5 mM $MgCl_2$ and 2 mM DTT). HMM or S1 fragments were separated from the precipitated material by centrifugation.

Actin was prepared from leg muscles of the rabbit as described by Pardee & Spudich (1982). Polymerized F-actin was fluorescence-labelled by incubating it overnight at 4°C with an excess of phalloidin-tetramethyl rhodamine isothiocyanate (Kron *et al*. 1991).

The correct orientation of the actin filament with respect to the myosin ensemble (Pertici *et al*. 2018; Pertici *et al*. 2020) was obtained by attaching the +end of the actin filament to the bead to form the BTA filament (Suzuki *et al*. 1996). BTA was prepared using the Ca^{2+}-insensitive gelsolin fragment TL40 (Hypermol) (Pertici *et al*. 2020) instead of gelsolin because it allows the nanomachine to be assembled in the absence of Ca^{2+}. TL40-coated beads were stored in the stock solution [150 mM NaCl, 20 mM sodium phosphate buffer, pH 7.4, 0.1 mM ATP, 10 mg mL^{-1} BSA, 5% (v/v) glycerol and 3 mM NaN_3] at 0°C for ∼6 months.

IVMA

The functionality of the purified motors was preliminarily tested by an IVMA, measuring the sliding velocity (V_f) of

actin filaments on a bed of the HMM under investigation. The IVMA was performed as described by Elangovan (2012), at room temperature (~24°C) and at ~60 mM ionic strength. The composition of the experimental solution for the IVMA was: saturating MgATP (2 mM), 25 mM imidazole, pH 7.4, 30 mM KCl, 2 mM EGTA, 4 mM $MgCl_2$, 10 mM DTT, 20 μg mL^{-1} catalase, 100 μg mL^{-1} glucose oxidase and 5 mg mL^{-1} glucose. Then, 0.8% methylcellulose (w/v, 400 cps) was added to the flow cell to prevent the lateral diffusion of the actin filaments by increasing the solution viscosity (Uyeda *et al.* 1990). The final desired values of free [Ca^{2+}], [Mg^{2+}] and [MgATP] were obtained using custom software similar to that already described by Brandt *et al.* (1972) and Goldman *et al.* (1984), as well as via Maxchelator (Bers *et al.* 2010). The concentration of frog HMM and S1 was 0.3 mg mL^{-1}, selected for maximum V_f. The same HMM concentration was used for the nanomachine experiments and was able to saturate the number of rupture events measured in the absence of ATP. The HMM concentration (0.3 mg mL^{-1}) is three-fold higher than that previously used for experiments with rabbit HMM (0.1 mg mL^{-1}) and is probably needed for the lower purification efficiency of the fully functional protein from frog muscle.

Dedicated software in LabVIEW (National Instruments, Austin, TX, USA) was used for actin filament tracking and velocity analysis. For every experiment, the mean value of V_f is obtained from filament tracking in at least four or five different zones. For a higher reproducibility of the data, the experiments were repeated at least four times for the same condition.

Steady-state ATPase assay

The actin-activated steady-state ATPase activities of rabbit HMM and frog HMM and S1 were measured by monitoring the rate of NADH absorbance decrease at 340 nm using a Multiskan FC Microplate Photometer (Thermo Fisher Scientific, Waltham, MA, USA), in assay buffer containing 25 mM Hepes, pH 7.4, 5 mM $MgCl_2$, 25 mM KCl and 0.5 mM DTT at 24 ± 1°C. Measurements started with the addition of 2 mM Na_2ATP. The amount of $CaCl_2$ to be added to achieve the desired free [Ca^{2+}] was calculated using Maxchelator (Bers *et al.* 2010). The concentration of HMM and S1 was 0.2 μM.

Mechanical measurements

The mechanical apparatus is described in detail in Pertici *et al.* (2018). Briefly, the myosin motors are deposited on the functionalized surface of a chemically etched single-mode optical fibre with a diameter ~4 μm. The fibre, carried on a three-way piezoelectric nanopositioner (nano-PDQ375; Mad City Lab, Madison WI, USA) that acts as a displacement transducer, is brought to interact with an actin filament attached, with the correct orientation, to a bead trapped in the focus of a DLOT that acts as a force transducer. The assembly of the nanomachine and the characteristics of the force and displacement transducers have been described in detail previously (Pertici *et al.* 2018). For all of the experiments, HMM from frog hindlimb (concentration 300 μg mL^{-1}) was dissolved in buffer A (25 mM imidazole, pH 7.4, 30 mM KCl, 2 mM EGTA, 4 mM $MgCl_2$, 10 mM DTT and 2 mM ATP, with or without 0.1 mM $CaCl_2$) (Pertici *et al.* 2018). Single bead-attached actin filaments, at least 6–7 μm long, were selected. To start the experiment, buffer B (buffer A plus 0.1 mg mL^{-1} glucose oxidase, 20 μg mL^{-1} catalase and 5 mg mL^{-1} glucose plus 0.5% w/v methylcellulose, 400 cP) was flowed at 10 μL min^{-1}. The presence of methylcellulose inhibited the lateral diffusion of F-actin (Uyeda *et al.* 1990), thereby minimizing the probability that, in 2 mM ATP, the interaction terminates during low-force isotonic contractions or during the initial phases of force redevelopment following large releases. The 0.5% w/v methylcellulose did not affect the mechanical and kinetic properties of the nanomachine (Pertici *et al.* 2018). All of the experiments were conducted at room temperature (23°C).

Data analysis

The velocity of shortening (V, μm s^{-1}) in the responses to reduction of force to F values (pN) below the isometric value (F_0) was measured by the slope of the displacement trace during the steady value of F. The F–V data were fitted with the hyperbolic Hill equation (Hill, 1938): $(F + a)\cdot(V + b) = (P_0 + a)\cdot b$, where a and b are the distances of the asymptotes from the ordinate and abscissa, respectively; a is a parameter that is used to express the degree of curvature of the relationship and has the dimension of a force (pN). When normalized for F_0, a is an index of the relative maximum power that can be delivered at intermediate forces (Hill, 1938). The power output (P) at any force was calculated as the product between F and V and expressed as μm $s^{-1}\cdot$pN $= 10^{-18}$ W = aW. Dedicated programs written in LabVIEW (National Instruments) and Origin 2015 (OriginLab Corporation, Northampton, MA, USA) were used for the analysis. All data are expressed as the mean ± SD unless otherwise stated.

Mechano-kinetic model

The results were numerically simulated with a stochastic model (Pertici *et al.* 2018) that estimates the probability distributions of potential results by allowing for random

variation in inputs over time until the SD of the result is lower than 5%. The mechanical cycle of the motors is depicted in Fig. 1. The state transitions, as well as the strain of the attached motors, are stochastically determined according to the kinetic scheme defined in Fig. 6 and Table 2. Each attached motor exerts, on the actin filament, a force that depends on its conformation and its relative position with respect to the actin monomer to which it is attached. The model operates either in position or force clamp. The iteration time in the calculation of the dependent variable, Δt ($= 10^{-5}$ to 10^{-6} s), depends on the stiffness of the system, which is mainly dictated by the trap compliance. Both the force generated by the motors (as transmitted by the BTA) and the force of the optical trap act on the trapped bead. The motion of the bead was simulated with over-damped dynamics by using a drag coefficient that was calculated according to the bead radius and the viscosity of the medium, determined by the presence 0.5% methylcellulose. In this way, the bead displacement in response to a stepwise change in force showed a rise time t_r similar to that measured experimentally (20 ms).

Results

The performance of the nanomachine powered by myosin motors from frog skeletal muscle is sensitive to Ca^{2+}

The mechanical output of the synthetic nanomachine powered by HMM fragments purified from frog hindlimb muscles was measured either in the absence of Ca^{2+} or in the presence of Ca^{2+} ($[CaCl_2] = 0.1$ mM, corresponding to 77 μM free Ca^{2+}). The motor ensemble, carried on the piezo-nanomanipulator acting as a length transducer, is brought to interact with an actin filament attached with the proper polarity to the bead trapped on the focus of DLOT acting as a force transducer, as detailed in the Methods (Fig. 2*A*). In the experiment shown in Fig. 2*B*, in which $[Ca^{2+}]$ is 0.1 mM, following the formation of the acto–myosin interface under position clamp (time interval, i_t, 1), after some sporadic interactions during which the force (blue) increases intermittently, the force increases to the isometric steady value F_0 of ~22 pN. When the control is switched to force clamp (i_t 2), because the applied force (25 pN) is larger than F_0, actin filament sliding (L, red) occurs in the lengthening direction at very low velocity. The following staircase of force drops from 25 to 20 (i_t 3), 15 (i_t 4), 10 (i_t 5) and 5 pN (i_t 6) elicits shortenings at a constant velocity that increases with the reduction of force. In i_t 7, the velocity reduces as the motor support approaches (and eventually touches) the trapped bead.

The frequency distribution of F_0 obtained from 33 experiments in 0.1 mM $CaCl_2$ (Fig. 2*C*, light grey bars) holds a mean value of 15.25 ± 6.31 pN. In 19 experiments performed in Ca^{2+}-free solution (dark grey bars), F_0 shows a frequency distribution shifted to the left with respect to that obtained in 0.1 mM $CaCl_2$ and a mean value (10.20 ± 4.748 pN). The reduction of F_0 (−30%) in the absence of Ca^{2+} is significant ($P = 0.004$).

In Fig. 2*D* the *F*–*V* relationship obtained in the presence of Ca^{2+} (grey circles, error bars are the SEM from 33 experiments) is compared with that obtained in Ca^{2+}-free solution (black circles, from 19 experiments). In either case, no points could be collected for forces <0.2 F_0 because the interaction between the motor ensemble and the actin filament was systematically lost at these low forces. The dashed lines (grey for 0.1 mM $CaCl_2$ data, black for Ca^{2+}-free data) are the fits to the respective *F*–*V* points of Hill's hyperbolic equation (Hill, 1938):

$$(F + a) \times (V + b) = (F_0 + a) \times b \qquad (1)$$

where the parameter a is the distance from the vertical asymptote to the ordinate, the parameter b is the distance from the horizontal asymptote to the abscissa and

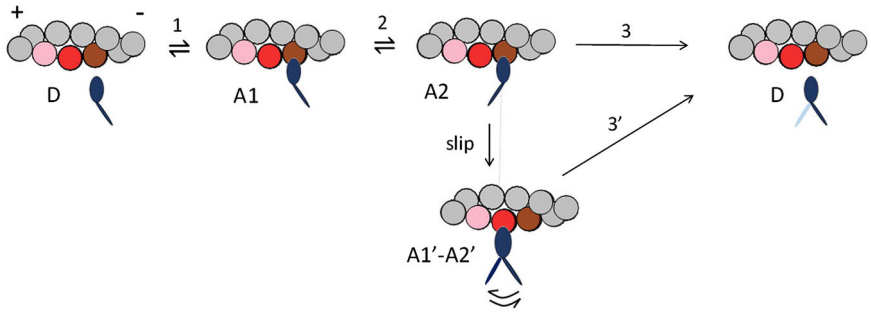

Figure 1. Kinetic scheme
States of the myosin motor (blue): D, detached state; A1 and A2 are states attached to one monomer of actin filament (brown) before and after the force generating step, respectively. During shortening the attached motor in A2 can slip to the next actin monomer (red) farther from the centre of the sarcomere; a second slipping to the pink monomer has a probability of 10% of that of the first slipping. Reproduced from Pertici *et al*. (2018).

$b \cdot F_0/a$ is the ordinate axis intercept that estimates the maximum shortening velocity (or the velocity of unloaded shortening), V_0. V_0 is 4.60 ± 1.14 μm s^{-1} in the presence of Ca^{2+} and 6.42 ± 2.64 μm s^{-1} in Ca^{2+}-free solution, showing a ∼40 % increase in the absence of Ca^{2+} but, given the variation and paucity of data collected at low forces (<0.3 F_0), the difference is not significant (P = 0.46). As shown in detail in Fig. 3, a similar, this time significant, potentiating effect by Ca^{2+}-free solution is found for V_f, the velocity of actin sliding over frog HMM in the IVMA (filled circles on the ordinate in Fig. 2*D*). This result solidifies the conclusion that V_0 increases in the absence of Ca^{2+}. Both in the presence and the absence of Ca^{2+}, V_0 is similar to V_f (Table 1), whereas, *in situ*, in single fibres from the same frog muscle, V_0 was found to be much larger than V_f (Elangovan *et al.* 2012).

The combined effects of Ca^{2+}, potentiation of the high load force, depression of the unloaded shortening velocity and reduction of the curvature of the *F–V* relationship, result in a Ca^{2+}-dependent increase in the power developed at high and intermediate loads with a maximum power (P_{max}) that increases from 6.29 ± 0.69 aW in Ca^{2+}-free solution (Fig. 2*E*, black) to 7.61 ± 0.56 aW in 0.1 mM $CaCl_2$ (grey) (P = 0.17).

Ca^{2+} depresses the kinetic parameters of frog myosin measured in the IVMA and in solution

The kinetic parameter of the actin–myosin ATPase cycle underlying V_0 is the rate of detachment of myosin motors following the execution of the working stroke (Huxley, 1957; Woledge *et al.* 1985; Piazzesi & Lombardi, 1995; Smith & Geeves, 1995). At low load (and high shortening speed), the working stroke is very fast and the rate limiting step in the cycle is detachment.

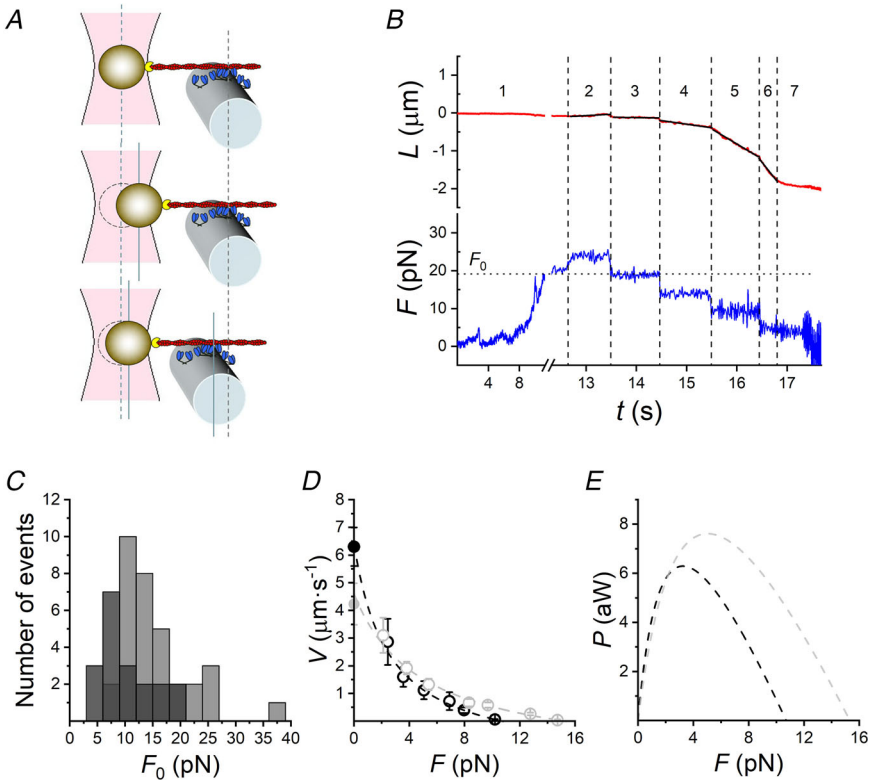

Figure 2. Performance of the frog HMM-based nanomachine
A, schematic representation of three snapshots during the interaction between the actin filament and the motor ensemble. Upper: position clamp, just before interaction; middle: position clamp at F_0; lower: force clamp at 0.4 F_0. *B*, recording of actin filament sliding (*L*, upper trace, red) and force (*F*, lower trace, blue) during an interaction. Numbers bounded by dashed lines identify the time intervals (i_t) as detailed in the text. *C*, frequency distribution of F_0. Data from 33 experiments performed in 0.1 mM $CaCl_2$ (= 77 μM free [Ca^{2+}], light grey bars) and 19 experiments performed in Ca^{2+}-free solution (dark grey bars), plotted in classes of 3 pN. The overlapping portion of each bar is marked by an even darker grey. *D*, *F–V* relationships. Open grey circles, 0.1 mM $CaCl_2$; open black circles, Ca^{2+}-free solution. Points are the mean ± SEM from individual experiments, grouped in classes of force 0.15 F_0 wide. The dashed lines are Hill's hyperbolic equation fits to the data with the same colour code as symbols. Filled circles on the ordinate are the corresponding V_f values: grey in 0.1 mM $CaCl_2$, black in Ca^{2+}-free solution. *E*, *P–F* relationships calculated from the *F–V* fits in (*D*), with the same colour code.

Table 1. Simulated mechanical and energetic parameters of the muscle half-sarcomere and nanomachine

Experimental model	F_0 (pN)	V_0 (μm s^{-1})	P_{max} (aW)	φ_0 (s^{-1})	φ_{Pmax} (s^{-1})	$r_{s,0}$ (s^{-1})	$r_{s,Pmax}$ (s^{-1})
Half-sarcomere							
$N = 294$	514 ± 29	16.57 ± 0.27	939	8.5	42.9	1.33	52.09
Nanomachine							
$N = 14$	10.7 ± 0.9	6.20 ± 0.95	6.4	27.6	33.2	34.33	42.87
$N = 36$	42.1 ± 2.0	8.19 ± 0.35	31.1	23.9	33.4	27.53	45.91

When possible, the parameters are accompanied by the references that provide the standard values used to constrain the simulation at the level of the muscle half-sarcomere. *N*, number of available motors, which, per half-thick filament, is 49 crowns × 6 motors per crown = 294 (Craig & Offer, 1976); F_0, isometric force estimated from the fit, which, for half-sarcomere, refers to the half-thick filament (Piazzesi *et al*. 2003); P_{max}, maximum power; V_0, maximum shortening velocity (Elangovan *et al*. 2012); φ_0 flux through step 1 of the cycle in Fig. 1 in isometric condition, corresponding to the ATP hydrolysis rate per myosin head at F_0: (Barclay, 2015); φ_{Pmax}, ATP hydrolysis rate per myosin head at P_{max} (Barclay *et al*. 2010; Barclay, 2015); r_s, slipping rate within the same ATPase cycle (step 'slip' in Fig. 1) in isometric condition ($r_{s,0}$) and at P_{max} ($r_{s,Pmax}$).

However, a stress-dependent accelerated detachment prevents attached motors from becoming negatively strained and generating a resisting load, in this way preserving the ability of fast skeletal muscle to shorten at high speed. Accordingly, the rate of the ATP hydrolysis increases with the reduction of the load for the strain-dependent increase in the rate of motor detachment (Kushmerick & Davies, 1969). Moreover, solution kinetic measurements of the rate of ATP hydrolysis by myosin extracted from different muscle types in which V_0 ranges by a factor of 10 were found to correlate to V_0 measured in the muscle of origin (Barany, 1967). This finding is a remarkable feature of muscle myosin II that works in an ensemble: independent of the muscle type, the velocity of unloaded shortening is maximized in relation to the ATP hydrolysis rate by keeping the duty ratio (i.e. the fraction of the ATPase

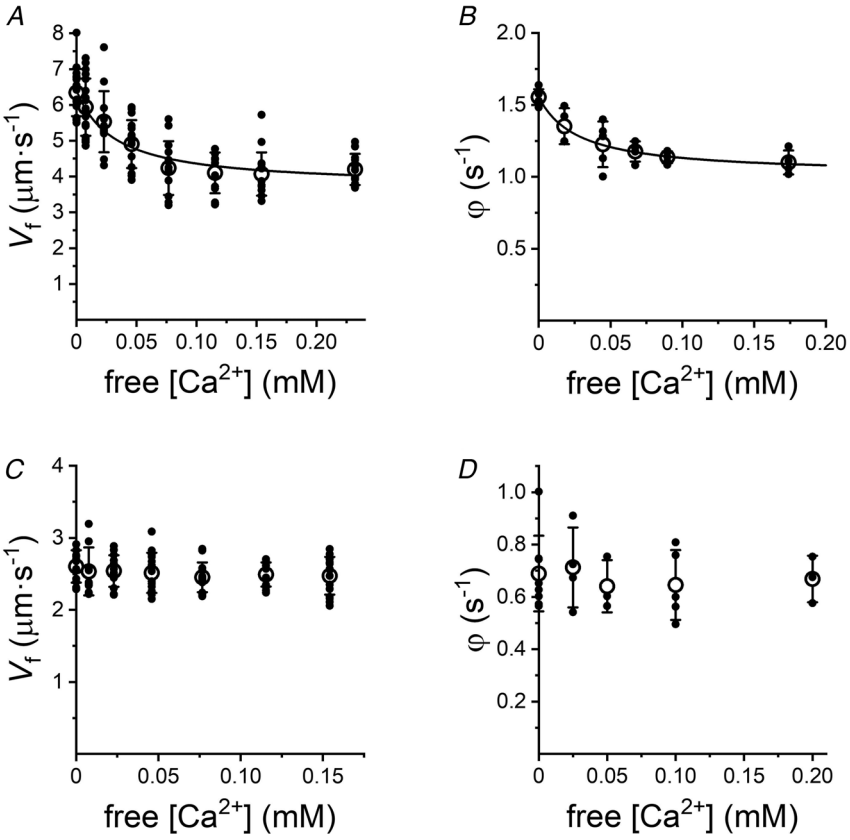

Figure 3. Ca^{2+} titration curves of V_f and rate of actin-activated ATPase activity φ of frog and rabbit HMM
All experiments were performed at 24°C. *A*, V_f with HMM from frog hindlimb muscles. Continuous line: hyperbolic fit to data, as detailed in the text. [HMM] is 0.3 mg mL^{-1}, ionic strength ∼60 mM. Ca^{2+} concentration is expressed as free [Ca^{2+}]. *B*, φ of HMM from frog muscle. [HMM] = 0.2 μM and [F-actin] = 40 μM. Continuous line: hyperbolic fit to data. *C*, V_f with HMM from rabbit psoas muscles. [HMM] is 0.1 mg mL^{-1}. *D*, φ of HMM from rabbit muscle. [HMM] = 0.2 μM and [F-actin] = 20 μM.

cycle time the myosin motor stay attached) as low as 0.05 (Tyska & Warshaw, 2002). Under these conditions, it is conceivable that the Ca^{2+}-dependent reduction for frog myosin of V_0 in the nanomachine and V_f in the IVMA is accompanied by the reduction in the actin-activated ATPase rate (φ) in solution kinetic experiments. Figure 3 shows the titration curves of the effects of Ca^{2+} on both V_f (Fig. 3*A*) and φ (Fig. 3*B*) of the HMM fragment from frog hindlimb muscles. The increase in [$CaCl_2$] from 0 to 0.2 mM (corresponding to 0–0.154 mM of free Ca^{2+}) induces a decrease in V_f (Fig. 3*A*) from a maximum value of 6.34 ± 0.66 μm s^{-1} in Ca^{2+}-free solution to a minimum value of 4.23 ± 0.75 μm s^{-1} (∼−30%, $P < 0.0001$) attained at 0.1 mM $CaCl_2$. The V_f – [Ca^{2+}] relation can be fitted by the hyperbolic equation:

$$V_f = V_{f,O} + c \times \left[Ca^{2+}\right] / \left(K_d + \left[Ca^{2+}\right]\right) \quad (2)$$

where $V_{f,0}$ is the V_f value in Ca^{2+}-free solution and ($V_{f,0} + c$) is the horizontal asymptote. K_d (i.e. [Ca^{2+}] for half-maximal inhibition) is 32 ± 13 μM.

Ca^{2+} titrations of φ over the same range of [$CaCl_2$] (Fig. 3*B*) show a decrease from 1.55 ± 0.05 s^{-1} in Ca^{2+}-free solution to 1.14 ± 0.04 s^{-1} (∼−27%, $P < 0.0001$), which is attained at 0.1 mM $CaCl_2$. Fitting the frog φ – [Ca^{2+}] relation with a hyperbolic equation similar to eqn (2), gives an estimate of K_d of 28 ± 4 μM, which is about the same as that found for V_f ($P = 0.8$).

Thus, the Ca^{2+} sensitivity of the nanomachine performance powered by frog HMM is accompanied by an equivalent sensitivity of the related kinetic parameters in solution. Because the performance of the nanomachine powered by rabbit psoas HMM is not affected by Ca^{2+} (Pertici *et al.* 2020), testing the Ca^{2+}-sensitivity of the related mechano-kinetic parameters of rabbit HMM is straightforward. Indeed, neither V_f (2.60 ± 0.22 μm s^{-1} in Ca^{2+}-free solution) (Fig. 3*C*), nor φ (0.69 ± 0.14 s^{-1} in Ca^{2+}-free solution) (Fig. 3*D*) are significantly affected by [Ca^{2+}] in the same range as that used for titrating Ca^{2+} action on frog HMM.

Molecular basis of the Ca^{2+} sensitivity of frog myosin

The nanomachine is assembled at the lowest level of organization of the motile system, consisting of an ensemble of purified HMM fragments of muscle myosin from either frog (present study) or rabbit muscle (Pertici *et al.* 2020), brought to interact with an unregulated actin filament prepared in the same way from rabbit muscle. Under these conditions, the only source of the functional class-diversity for to the Ca^{2+}-sensitivity must be in the HMM. A divalent cation binding site has been found in the RLC of skeletal muscle myosin of vertebrates (Bagshaw & Reed, 1977). To investigate whether this domain is responsible for the Ca^{2+}-sensitivity of frog HMM, we performed IVMA and ATPase measurements on frog myosin motors after removal of the RLC. Chymotryptic digestion of myosin molecules is known to produce an S1-like fragment that lacks the RLC but is still able to move actin filaments *in vitro* (Weeds & Taylor, 1975; Ferenczi *et al.* 1978; Toyoshima *et al.* 1987). We adapted the protocol to generate a frog S1-like fragment missing the RLC (Fig. 4*A*). When the S1-like fragment of frog myosin is used to coat the nitrocellulose surface of the IVMA experiments, V_f is 1.65 ± 0.25 μm s^{-1} in Ca^{2+} free solution (∼1/4 of the value obtained with frog HMM) and the results are insensitive to the presence of Ca^{2+} over the entire range of Ca^{2+} concentrations (Fig. 4*B*). Similarly, φ measured with the S1-like fragment of frog myosin ($= 3.17 \pm 0.78$ s^{-1} in Ca^{2+}-free solution; twice the value obtained with frog HMM) is insensitive to [Ca^{2+}] (Fig. 4*C*). Thus, the sensitivity of frog HMM to Ca^{2+} is the result of a Ca^{2+}-binding site in the portion of the HMM removed by chymotryptic digestion, probably the divalent cation-binding site found in the RLC of rabbit skeletal muscle myosin (Weeds & Taylor, 1975). Notably, V_f and φ measured in rabbit HMM did not show the same Ca^{2+} sensitivity as frog HMM, in agreement with the absence of any effect of Ca^{2+} on the mechanical performance of rabbit HMM (Pertici *et al.* 2020). The finding that the S1-like fragment of frog myosin in Ca^{2+}-free solution exhibits a V_f that is much smaller than that of the corresponding HMM is consistent with previous work on rabbit myosin and should be related to a less favourable mode of surface attachment of the S1 fragment compared to HMM (Toyoshima *et al.* 1987).

Model simulation of the *in situ* and *in vitro* performance of frog muscle myosin

Here, a model simulation is described that is able to interface the performance of the nanomachine powered by HMM from frog hindlimb muscles with that of the muscle of origin. The kinetic scheme of actin–myosin interaction (Fig. 1) is the same as that used to explain the mechanics and energetics of the nanomachine powered by rabbit psoas HMM (Pertici *et al.* 2018; Pertici *et al.* 2020). The model is based on one detached state (D) and two different force-generating attached states (A1 and A2). Their stiffness is assumed 2.8 pN nm^{-1} (Piazzesi *et al.* 2007; Brunello *et al.* 2014). The kinetics of state transitions are first constrained to fit the mechanics and energetics of the frog hindlimb muscles and then scaled down to predict the performance of the ensemble of myosin motors working in the nanomachine.

The fundamental mechanical constraint for simulating the whole muscle performance at the same temperature as that of the nanomachine (23°C) is the *F*–*V* relationship (dashed line in Fig. 5*A*) calculated by the Hill hyperbolic

Table 2. Equations expressing the *d*-dependence of the rate constants of the forward and backward transitions in the model

k_1	$= (125/\chi/\sqrt{(2*\pi)})*\exp(-d^2/2*\chi^2) = 0$	$-2.5\ nm < d < 2.5\ nm$ $\lvert d\rvert \geq 2.5\ nm$
k_{-1}	$= ((32500)/\chi/\sqrt{(2*\pi)})*\exp(-d^2/2*\chi^2) = 0$	$-2.5\ nm < d < 2.5\ nm$ $\lvert d\rvert \geq 2.5\ nm$
k_2	$= 3800*\exp(-0.7*(d-2))/(1+\exp(-0.7*(d-2)))$	
k_{-2}	$= 280*\exp(0.7*(d+2))/(1+\exp(0.7*(d+2)))$	
k_3	$= (5100*\exp(-1.7*(d+6.45))/(1+\exp(-1.7*(d+6.45))))+40$	No Ca^{2+}
	$= (1000*\exp(-1.1*(d+6.45))/(1+\exp(-1.1*(d+6.45))))+23.5$	Ca^{2+}
k_3'	$= (5100*\exp(-1.7*(d+6.45))/(1+\exp(-1.7*(d+6.45))))+40$	$d \leq 2.68\ nm$, No Ca^{2+}
	$= (1000*\exp(-1.1*(d+6.45))/(1+\exp(-1.1*(d+6.45))))+23.5$	$d \leq 2.68\ nm$, Ca^{2+}
	$= \exp(2*(d-0.83))$	$d > 2.68\ nm$, No Ca^{2+}
	$= \exp(2*(d-1.1))$	$d > 2.68\ nm$, Ca^{2+}
k_{slip}	$= (14000/\chi/\sqrt{(2*\pi)})*\exp(-(d+5)^2/2*\chi^2) = 0$	$-7.5\ nm < d < -2.5\ nm$ $d \leq -7.5\ nm$, $d \geq -2.5\ nm$

$\chi = 1.8$ nm.

equation using published data at different temperatures and their relative Q_{10}: 1.26 for F_0, 2.3 for V_0 and 1.1 for a/F_0 (Woledge *et al.* 1985; Piazzesi *et al.* 2003; Elangovan *et al.* 2012). The resulting standard values that characterize the *F–V* relationship of the frog muscle at 23°C are: $V_0 = 16.5\ \mu m\ s^{-1}$, $F_0 \sim 290$ kPa and $a/F_0 = 0.35$. The force units in the abscissa of Fig. 5*A* are scaled per half-thick filament (htf), taking into account the thick filament density ($\sim 5.8 \times 10^{14}\ m^{-2}$) (Reconditi *et al.* 2014). The isometric force per half-thick filament, $F_{0,htf}$, is ∼500 pN. The corresponding *P–F* relationship is shown by the dashed line in Fig. 5*B* and the maximum power, attained at ∼1/3 $F_{0,htf}$, is ∼950 aW.

Model simulations of the *F–V* and *P–F* relationships per htf (continuous lines in Fig. 5*A* and *B*, respectively) are obtained by adjusting the specific rate functions governing the kinetics of state transitions (Fig. 6 and Table 2). The coupling between mechanical and biochemical steps in the cycle of Fig. 1 has been already described in detail (Pertici *et al.* 2018). The underlying energetics (Fig. 5*C* and Table 1) is a further constraint according to data in the literature, as detailed below.

Detached motors (D) attach to the actin monomer (5 nm in diameter) (D→A1, step 1 in Fig. 1) at values of *d* (the relative axial position between the motor and the actin monomer with $d = 0$ when the force in A1 is zero) ranging from −2.5 to 2.5 nm, according to the principle of the nearest-neighbour interaction. The working stroke that accounts for the generation of force at $d = 0$ and its maintenance during shortening within the size of the working stroke (Huxley & Simmons, 1971; Piazzesi & Lombardi, 1995) is a result of the transition A1→A2

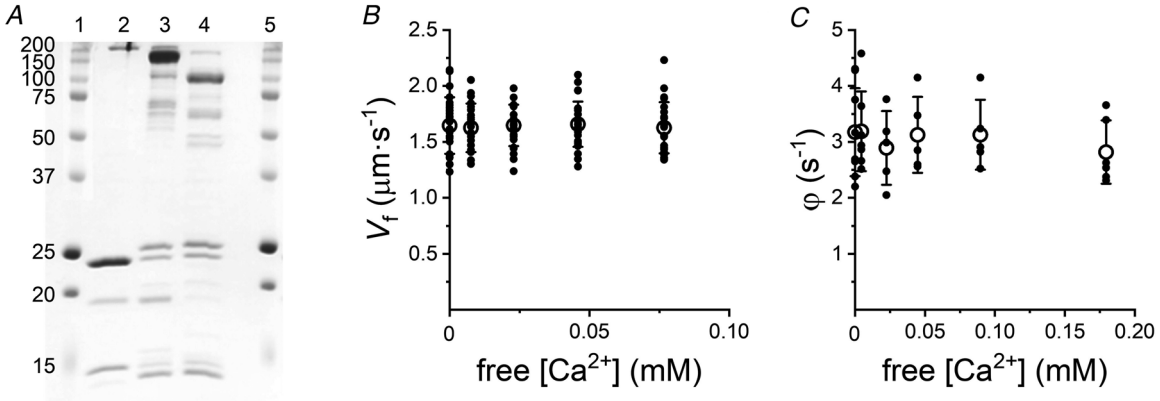

Figure 4. Effect of Ca^{2+} on the kinetic parameters of RLC-free S1 purified from frog skeletal muscle
A, SDS-PAGE (15%) showing proteins purified from frog skeletal muscle. Lanes 1 and 5: protein markers. Lane 2: full-length myosin purified from frog skeletal muscle. Lane 3: HMM fragment. Lane 4: S1 fragment devoid of RLC (the band in correspondence of 20 kDa is lost), obtained by chymotryptic digestion of myosin in the presence of EDTA (Weeds & Taylor, 1975). *B*, Ca^{2+} titration curves for V_f in the IVMA using the chymotryptic S1 fragment ([S1] = 0.8 mg mL^{-1}, ionic strength ∼60 mM, Temperature = 24°C). *C*, Ca^{2+} titration curves of φ of frog S1, measured at 24°C with [S1] = 0.2 μM and [F-actin] = 40 μM.

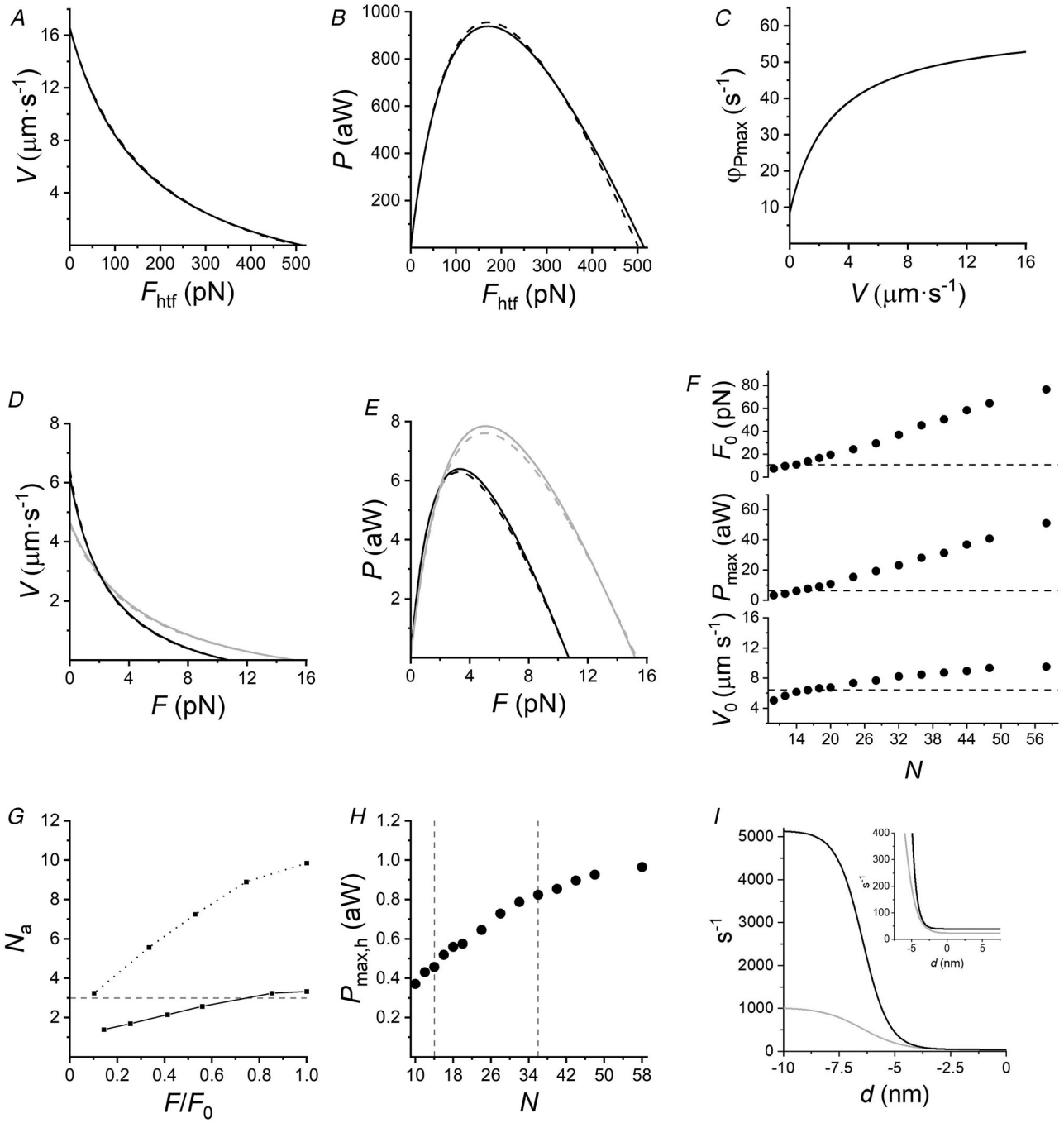

Figure 5. Model simulation of *in situ* and *in vitro* mechanics and energetics of frog myosin
A–C, data for the muscle. *A*, *F–V* relationship obtained by fitting the Hill equation to data of frog muscle (dashed line) and superimposed model simulations (continuous lines). Data on the ordinate normalized for the half-sarcomere length, F_{htf} is the force per half-thick filament. *B*, *P–F* relationship obtained from (*A*), with lines coded as in (*A*). *C*, Relationship between the rate of ATP hydrolysis per motor (φ) and the shortening velocity. *D–E*, *F–V* and *P–F* relationships, respectively, determined with the nanomachine (dashed lines) powered by frog HMM in Ca^{2+}-free conditions (black) and in the presence of Ca^{2+} (grey) (from Figs 2*D* and 2*E*), with superimposed model simulations (continuous lines, same colour code). *F*, dependence on *N* of the three parameters featuring the nanomachine performance (F_0, P_{max}, V_0). The horizontal dashed lines are the respective experimental values. *G*, relationship between number of attached heads (N_a) and force relative to F_0 calculated with the model for the frog nanomachine with $N = 14$ (continuous line) and 36 (dotted line); the horizontal dashed line is drawn for $N_a = 3$. *H*, dependence on *N* of the power per myosin head ($P_{max,h}$). Vertical dashed lines correspond to $N = 14$ and 36. *I*, dependence of the rate function k_3 on *d* (as defined in the text) for the nanomachine in the absence of Ca^{2+} (black) and in the presence of Ca^{2+} (grey). Inset: expanded region of the relationship.

(step 2). In isometric contraction, the rate-limiting step in the cycle is detachment from A2, the rate of which remains low for d up to −5 nm (Fig. 6): under these conditions, the fraction of attached motors (the duty ratio r) is maximum (r_0), at 0.23 for the muscle of *Rana esculenta* (Brunello *et al.* 2014), whereas the rate of ATP splitting per myosin head (φ_0) is minimum (∼9 s^{-1} at room temperature) (Barclay, 2015). During steady shortening, r decreases and the ATP splitting rate per myosin head (φ) increases (Fig. 5*C*) as a result of the increase in the rate of motor detachment following the working stroke (Huxley, 1957; Piazzesi & Lombardi, 1995; Nyitrai & Geeves, 2004; Caremani *et al.* 2013). However, φ at the load for the maximum power (φ_{Pmax}) is higher than φ_0 by no more than four- or five-fold in frog muscle (Barclay *et al.* 2010; Barclay, 2015), so that the resulting maximum power can be predicted only by assuming that, during shortening, the attached myosin motors can rapidly regenerate the working stroke during the same ATPase cycle by slipping to the next actin farther from the centre of the sarcomere (Piazzesi & Lombardi, 1995; Lombardi *et al.* 1992; Caremani *et al.* 2013) (step 'slip' in Figs 1 and 6*C*) and undergoing A1′–A2′ state equilibration according to step 2 kinetics (Huxley & Simmons, 1971). Detachment from either A1′ or A2′ (step 3′) implies ATP hydrolysis.

As shown in Figs 5*A*–*C* and Table 1, the relationships and the underlying mechanical and energetic parameters predicted for the muscle half-sarcomere agree with those derived from published data (Barclay *et al.* 2010; Barclay, 2015). Notably, the ATP splitting rate per myosin head at F_0, φ_0, calculated by the flux through step 1, is 8.5 s^{-1}, whereas, at P_{max} (φ_{Pmax}), it increases to 42.9 s^{-1} ($5 \times \varphi_0$).

The simulation of the performance of the frog-HMM nanomachine implies taking into account the methodological limits of the *in vitro* mechanical system, as already described for the rabbit-HMM nanomachine (Pertici *et al.* 2018; Pertici *et al.* 2020): (i) the compliance in series with the system must be raised by two orders of magnitude to include the trap compliance, 3.7 nm pN^{-1}, and (ii) the random orientation of the motors on the support reduces the average force (Ishijima *et al.* 1996) and length step size (Tanaka *et al.* 1998) developed during an interaction. The limits as a result of the random orientation are introduced in the model simulation by reducing, progressively with the deviation from the correct orientation (0°), the isometric force and the shortening range within which an attached force generating motor (A2 state) maintains force, according to the family of A2 force functions shown in Fig. 7 (pink lines). The relevant parameters describing the force function range from F_c = 7.5 pN and L_c = 10 nm, exhibited by a correctly oriented motor (black line), to 0.75 pN and 1.5 nm, respectively (red line), exhibited by a motor rotated by 180° from the correct orientation. Correspondingly, the slope of the A1 force function, representing the stiffness of the attached motor, scales from 2.8 pN nm^{-1} (black dashed line) to 0.28 pN nm^{-1} (red dashed line). This assumption is realistic considering that, for a motor away from the correct orientation, the S2 domain also can contribute to the compliance (Kaya & Higuchi, 2010; Linari *et al.* 2020).

The performance of the nanomachine powered by frog HMM is Ca^{2+}-sensitive. Because in the *in vivo* contraction the rise of [Ca^{2+}] never exceeds 5 μM (Caputo *et al.* 1994), which means that it remains around six-fold lower than the K_d measured in the Ca^{2+} titration experiments (Fig. 3*A* and *B*), the control condition for the nanomachine (i.e. to be directly related to the frog muscle performance) must be that in the absence of Ca^{2+}.

Under these conditions, the kinetic scheme in Fig. 1 is able to fit both the *F*–*V* relationship (Fig. 5*D*, black dashed

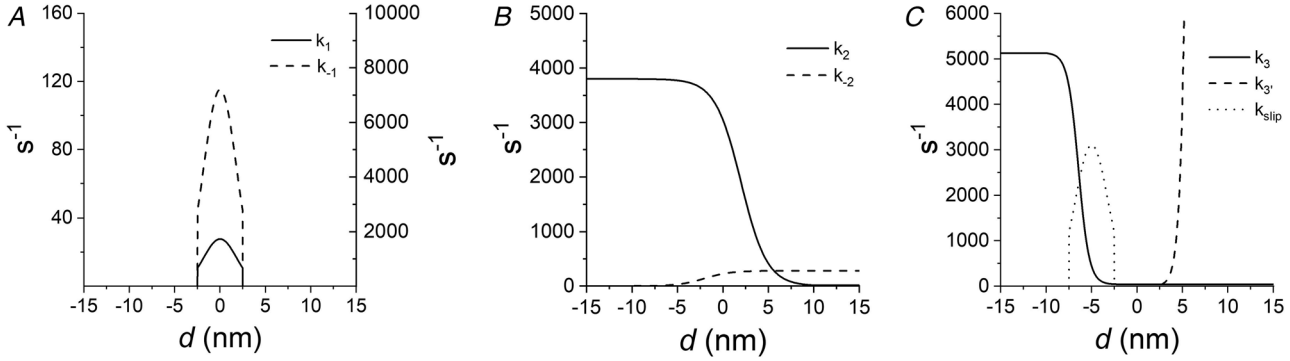

Figure 6. Dependence on *d* of the rate functions for the state transitions
d is the relative position between the motor and the actin monomer, taken as zero when the motor in the A1 state exerts zero force. In each case, k_i and k_{-i} are the forward and backward rate constants of the *i*th step. *A*, step 1, attachment reaction, k_1 continuous line, left ordinate; k_{-1} dashed line, right ordinate. *B*, step 2, force generating transition, k_2 continuous line, k_{-2} dashed line. *C*, step 3, detachment reaction, k_3 continuous line. The slipping of A2 to the next actin farther from the centre of the sarcomere is governed by k_{slip} (dotted line). Detachment from an attached state following slipping, $k_{3'}$ (dashed line) superimposes to k_3 for $d \leq 2.68$ nm.

line: experiment, black continuous line: model) and *P*–*F* relationship (Fig. 5*E*, black dashed line: experiment, black continuous line: model) once the number of motors available for the actin interaction (N) is scaled down conveniently from that in the half-thick filament, 294 (Craig & Offer, 1976), to 14. The optimization of the fit by the scaling procedure is shown in detail in Fig. 5*F*, where the relevant parameters of the nanomachine performance (F_0, P_{max} and V_0) predicted by the model are plotted in relation to N (circles), whereas the dashed lines identify the experimental values. The best fit is obtained for $N = 14$.

An independent estimate of N can be obtained by recording the number of rupture events in the absence of ATP when frog HMM at the same concentration (0.3 mg mL^{-1}) as that used for the experiments in physiological ATP is dispersed on the same support, according to the method described in detail in Pertici *et al.* (2018). The number of rupture events in 20 experiments was 7.05 ± 2.67. Assuming that each motor of the myosin dimers identified as available for actin interaction by rupture events in rigor behaves independently in 2 mM ATP, seven rupture events in rigor imply $N = 14$, in agreement with the prediction of the model. It must be noted that N estimated by either procedure with frog myosin HMM is 15% less than that estimated on the same support when the nanomachine is made by psoas rabbit HMM (16) (Pertici *et al.* 2018), probably as a consequence of the larger fragility of frog myosin.

The simulation suggests that, in the region of N values lower than 40, V_0 decreases with the reduction of N with a progressively increasing slope. In this respect, it must be noted that V_0 should be intrinsically independent of the number of available motors and solely dependent on the rate constant for motor detachment (Huxley, 1957).

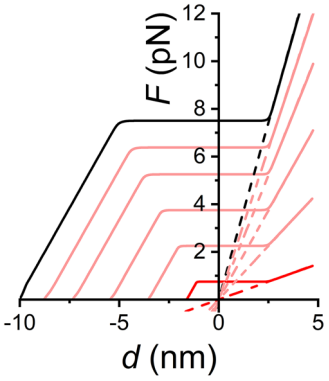

Figure 7. Force profile of the attached states of the motor as a function of *d*
A1 state, dashed line and A2 state, continuous line. Black, force profile of correctly oriented motors; red, force profile of motors 180° away from the correct orientation; pink, four profiles corresponding to four intermediate motor orientations.

The decrease in V_0 for $N < 40$ can be explained taking into account that (i) the duty ratio decreases with the increase in shortening velocity; (ii) under the above condition, there is a threshold value of N below which, during low load shortening, the number of attached motors (N_a) becomes lower than the critical value that ensures the conditions for continuous interaction, such that at least one motor is attached at any time (Uyeda *et al.* 1990); and (iii) with the reduced speed of lateral diffusion of the actin filament as a result of the presence of 0.5% methylcellulose, the loss of continuous interaction appears as a reduction in the average sliding velocity (Pertici *et al.* 2018). As shown in Fig. 5*G*, for $N = 36$, N_a remains above 3 for any *F*–*V* point, also for unloaded shortening, whereas, when $N = 14$, N_a decreases to <3 even during shortening at moderate velocity (high load). Under this condition, the *F*–*V* points are further depressed with respect to the depression as a result of the random motor orientation. This effect also explains the finding that V_0 of the nanomachine is similar to V_f (Fig. 2*D*), in contrast to the evidence that V_0 from an intact fibre is almost twice as large than V_f (Elangovan *et al.* 2012). Another consequence of the limited number of available motors becomes evident by plotting the maximum power per myosin head ($P_{max,h}$, calculated as P_{max}/N) *vs.* N (Fig. 5*H*). For $N = 14$, $P_{max,h}$ is ∼50% the maximum value, which is attained for N >36, the minimum value of N for which N_a remains >3 at any load (Fig. 5G, dotted line). The value of V_0 predicted by the model for $N = 36$ is 8.4 ± 0.5 μm s^{-1}, which is ∼35% larger than that of the nanomachine (Table 1). V_0 is still depressed by a factor of two with respect to the muscle value (16.4 ± 0.3 μm s^{-1}) (Fig. 5*A* and Table 1) as a consequence of the random motor orientation in the nanomachine.

Strikingly, the model simulation satisfactorily predicts the depressed responses of the nanomachine with respect to the muscle (continuous lines in Fig. 5*A*, *B*, *D* and *E*), providing the key to understand the underlying reasons.

Kinetic requirements to fit the Ca^{2+}-sensitivity of frog myosin nanomachine

The performance of the nanomachine powered by frog HMM is Ca^{2+} sensitive (Fig. 2): addition to the solution of 0.1 mM $CaCl_2$, which is able to saturate the kinetic effects of Ca^{2+} (Fig. 3*A* and *B*), induces changes in the isometric force (Fig. 2*C*) and in the *F*–*V* relationship (Fig. 2*D*, black Ca^{2+}-free, grey 0.1 mM Ca^{2+}). F_0 increases by 43%, V_0 reduces by 28% and P_{max} increases by 21% (Fig. 2E). These effects are reproduced by the model (Fig. 5*C* and *D*, dashed lines: experiment, continuous lines: model) following a general reduction of the rate constant for motor detachment at the end of the working stroke (k_3 and k_3'). This is shown in Fig. 5*I*, where the

rate function in the presence of 0.1 mM Ca^{2+} (grey curve) is superimposed on that in Ca^{2+}-free solution (black curve from Fig. 6*C*). The Ca^{2+}-dependent changes of the detachment rate constant, detailed in the corresponding equations in Table 2, consist of halving the steady value at *d* around zero, a 35% reduction of the slope of rise at negative *d* and a five-fold reduction of the maximum value attained at the most negative *d* values.

Discussion

In the present study, the emergent properties of an ensemble of myosin molecules extracted from fast skeletal muscle of the frog hind limb are investigated using the synthetic nanomachine first demonstrated using myosin from fast mammalian skeletal muscle (rabbit psoas) (Pertici *et al*. 2018; Pertici *et al*. 2020). The nanomachine mimics the properties of the half-sarcomere in its simplest composition, namely when it comprises only the contractile proteins myosin and actin, and thus in the absence of the effects of the other sarcomere (regulatory, accessory and cytoskeleton) proteins. Under these conditions, the features of the nanomachine are fully accounted for by the class-specific fast myosin isoform of the frog (which is an orthologue isoform of the rabbit psoas myosin). The frog myosin has been chosen in the present study, despite its fragility at room temperature, because muscles and intact single fibres from frog hind limb provide the most complete and reliable set of data concerning *in situ* mechanical, kinetic and energetic parameters of muscle contraction (Hill, 1938; Huxley & Simmons, 1971; Ford *et al*. 1977; Woledge *et al*. 1985; Lombardi *et al*. 1992; Linari & Woledge, 1995; Piazzesi & Lombardi, 1995; Piazzesi *et al*. 2003; Piazzesi *et al*. 2007; Barclay *et al*. 2010; Elangovan *et al*. 2012; Barclay, 2015) that are necessary to constrain the model, which is able to interface *in vitro* and *in situ* results and provide a detailed molecular explanation at different hierarchical levels.

In the present version of the nanomachine, to preserve $[Ca^{2+}]$ as a free parameter, the actin filament is attached to the bead with the correct polarity using the Ca^{2+} independent gelsolin fragment TL40 (Pertici *et al*. 2020). This new method opens the possibility for the investigation, in specifically reconstituted systems, of the role of any other sarcomeric protein that acts via a Ca^{2+}-dependent mechanism. Here, the new method reveals that the nanomachine powered by frog HMM exhibits a Ca^{2+} sensitivity of the mechanical performance (Fig. 2). The presence of Ca^{2+} 0.1 mM in the perfusion solution produces an increase in F_0 (+50%) and P_{max} (+21%) and a decrease in V_0 (−27%) with respect to the values measured in Ca^{2+}-free solution. In the same range of $[Ca^{2+}]$ (from 0 to 0.1 mM), the velocity of actin sliding in the IVMA, V_f, reduces by 33% and the actin-activated ATPase in solution, φ, reduces by 27% (Fig. 3). The Ca^{2+}-sensitivity of the nanomachine powered by frog HMM in the absence of any other sarcomeric protein can only be attributed to a direct interaction of Ca^{2+} with a specific regulatory domain in the HMM, as also confirmed by the Ca^{2+}-dependent depression found for V_f and φ in solution being the same as that for V_0. The Ca^{2+}-sensitivity is lost when the kinetic parameters are measured on the S1-fragment of the myosin deprived by the RLC (Fig. 4), suggesting that the structural basis of the Ca^{2+} action resides in the divalent cation binding site on the RLC of skeletal muscle myosin, as reported by Bagshaw & Reed (1977). Mammalian skeletal muscle myosin, instead, does not show any Ca^{2+}-sensitivity, neither for the mechanical parameters of the nanomachine (Pertici *et al*. 2020), nor for the kinetic parameters (Fig. 3*C* and *D*). In this respect, the frog myosin Ca^{2+}-sensitivity does not appear to play any evident physiological role during muscle contraction, considering that, in the muscle at rest ($[Ca^{2+}] \sim 10^{-7}$ M), the RLC divalent cation-binding site is mainly occupied by Mg^{2+} and its displacement by Ca^{2+} during muscle activation is almost zero because of the very slow rate of Mg^{2+}–Ca^{2+} exchange in relation to the duration of activation (Bagshaw & Reed, 1977) and the six-fold greater K_d of the Ca^{2+} effect (~30 μM) (Fig. 3*C* and *D*) with respect to the internal $[Ca^{2+}]$ attained in contracting frog muscle (5 μM in a twitch and only ~30% higher in a tetanus) (Caputo *et al*. 1994). In any case, as far as any differences in the competitive effect of Mg^{2+} and Ca^{2+} in frog muscle with respect to mammalian muscle, it should be considered that the physiological intracellular free $[Mg^{2+}]$ in frog skeletal muscle is calculated to be 2.5 mM (Dawson *et al*. 1978), which is similar to free $[Mg^{2+}]$ in our assays (~1.7 mM in the nanomachine experiments). It has been reported for rabbit skeletal muscle that, with 20 μM Ca^{2+} (a value in the range of the internal $[Ca^{2+}]$ peak in contracting mammalian muscle) (Baylor & Hollingworth, 2012), Ca^{2+} binding decreases increasing $[Mg^{2+}]$ above 100 μM (Bremel & Weber, 1975); however, even with a free $[Mg^{2+}]$ of 1 mM, about one Ca^{2+} is bound for each myosin molecule. In conclusion, modulation of Ca^{2+} binding to myosin in the range of $[Ca^{2+}]$ used in the present study is not influenced by the $[Mg^{2+}]$ in our assays. Under these conditions, a class-specific Ca^{2+}-sensitivity by the frog HMM in relation to either the performance of the nanomachine or the *in vitro* kinetic parameters appears only as a vestigial mechanism to be identified in lower animals.

So far, a myosin-based mechanism of Ca^{2+} activation has been found only in the molluscan striated muscle, in which the thin-filament regulatory proteins are absent and Ca^{2+} acts as a regulator by specific bonds with the essential light chain of myosin (Szent-Gyorgyi, 1975; Fromherz & Szent-Gyorgyi, 1995). An indirect Ca^{2+} regulation

of myosin occurs in vertebrates via a Ca^{2+}-dependent increase in the degree of phosphorylation of the RLC. There are many observations suggesting a role for the RLC with respect to modulating skeletal and cardiac muscle contraction, although the exact mechanism of these processes is still unknown. The activation of the Ca^{2+}/calmodulin-dependent myosin light chain kinase as a result of an increase in $[Ca^{2+}]$ during contraction leads to the phosphorylation of the RLC. In skeletal muscle, RLC phosphorylation induces an increase in the Ca^{2+} sensitivity of ATPase activity and force development (Szczesna *et al*. 2002). A phosphorylated RLC of the frog HMM used in our assays could explain the difference in Ca^{2+} sensitivity between frog HMM and the S1 fragment. Moreover, it would be interesting to test whether different degrees of phosphorylation of mammalian and frog HMM could be related to different Ca^{2+} effects. In cardiac muscle, RLC phosphorylation is known to control the myosin head conformation regulating the interaction between the myosin head and the thick filament (Kampourakis & Irving, 2015). Moreover, mutations in ventricular RLC leading to a reduction in phosphorylation levels and/or to a reduction of the affinity for Ca^{2+} are associated with the development of hypertrophic cardiomyopathy (Sczcesna *et al*., 2001).

The nanomachine performance is interfaced to that of the corresponding muscle using a model simulation with a unique kinetic scheme (Figs 1 and 6 and Table 2), which demonstrates the ability of the nanomachine to recapitulate the emergent properties of the muscle of origin and identifies the myosin-based functional diversity of muscles of animals with different orthologue isoforms of myosin. The effects of Ca^{2+} on the mechanical parameters of the frog nanomachine, namely the increase in F_0 and P_{max} and the decrease in V_0, are explained by the model simply via a Ca^{2+}-dependent reduction in the rate constant of motor detachment at the end of the working stroke (k_3). As shown in Fig. 5*I*, the only modification to fit Ca^{2+} effects consists of halving the value of the rate constant in the range of d values occupied by attached motors in isometric contraction and shifting, to a more negative strain, the value of d at which the rate constant of motor detachment exhibits a steep increase.

From the application of the model simulation, some outstanding features emerge:

(1) The kinetic scheme is able to identify the isoform-dependent kinetic features that underpin the difference in muscle performance. In comparison with fast skeletal mammalian muscle, at the same room temperature, frog muscle exhibits a two-fold larger V_0 and P_{max}: 16.57 μm s^{-1} and 939 aW per half-thick filament, respectively (Table 1), whereas the values for the mammalian muscle are 8.8 μm s^{-1} per half-sarcomere and 460 aW per half-thick filament, respectively (Pertici *et al*. 2018). These higher performances of frog muscle are fully accounted for by the model simulation (continuous lines, same colour code) by adjusting the relevant kinetic parameters of the frog myosin cycle, namely increasing, by three- to four-fold, the rate constants for motor attachment (k_1, k_{-1}) and force-generating transition (k_2, k_{-2}) together with increasing the rate constant of motor detachment (k_3 and k_3') for negative strains. It must be noted, however, that the working temperature of the two muscles *in vivo* is different (room temperature for the heterothermic frog and 35–37°C for the homeothermic mammal). Once the temperature sensitivity of the relevant rate constants is taken into account, the performance of the two muscles *in vivo* becomes quite similar.

(2) The same mechano-kinetic scheme selected for fitting the muscle performance is able to explain the mechanical performance of the nanomachine, once the methodological limits of the *in vitro* system are taken into account. The two important limits related to the design of the nanomachine are (i) the random orientation of myosin motors and (ii) the *in series* trap compliance that is two orders of magnitude larger than the *in series* compliance *in situ*. The effects of these limits on the nanomachine behaviour are either experimentally defined from previous approaches or formally treatable to be integrated in the model. The depressant effect of the random orientation of the motor on the force (Ishijima *et al*. 1996) and the length of the step size (Tanaka *et al*. 1998) are introduced in the model by scaling down, in proportion to the deviation from the correct orientation, the values of both d at which the A2 motors maintain the isometric force and the abscissa intercept of the A2 force function (Fig. 7). In this way, V_0 determined in the nanomachine is reproduced by the model, in turn demonstrating the power of the model with respect to interfacing single motor properties (the step size) with the properties emerging from its collective arrangement (V_0). The presence in the nanomachine of an *in series* compliance 100-fold larger than *in situ* causes the strain-dependent kinetics of the attached motors to generate the push–pull experienced by the attached motors when the addition–subtraction of the force contribution by each single motor induces actin sliding away from - toward the bead respectively (Pertici *et al*. 2018). As a consequence, the cycling rate of the motor ensemble is affected, as predicted by the model: with respect to the values in the corresponding muscle, the isometric ATPase rate φ_0 becomes three-fold larger (Table 1). The push–pull effect is reduced during isotonic contractions when φ increases with the reduction of the load (increase in the shortening velocity). At P_{max}, the nanomachine

exhibits a value of φ_{Pmax} smaller than that of the muscle (Table 1) as a consequence of the depression in the step size and thus in the low-load shortening velocity, as a result of the random orientation of motors.

The push–pull regime generated by the trap compliance affects the isometric response not only by increasing its energetic cost, but also by raising the probability of slipping of the attached motors to the next actin monomer (Fig. 1). Indeed, although, in the muscle, the slipping rate per motor predicted in isometric conditions ($r_{s,0}$) is 1.3 s^{-1}, which is only one-sixth of φ_0, in the nanomachine, $r_{s,0}$ becomes comparable to φ_0.

(3) Another striking feature of the model is the ability to predict the reasons of the limits of the nanomachine when it fails to achieve the expected performance. In the nanomachine powered by frog myosin, the combination of the low isometric duty ratio (0.23) and the low number of motors available for actin interaction ($N = 14$) causes, even during shortening at moderate velocity (high load), the average number of motors attached to actin at any time (N_a) to decrease to <3 (Fig. 5*G*, continuous line), which is the minimum predicted for ensuring continuous interactions between the myosin ensemble and the actin filament (Uyeda *et al*. 1990; Pertici *et al*. 2018). Under this condition, the *F–V* points are further depressed with respect to the depression as a result of the random motor orientation.

The above analysis is a striking demonstration of the power of the multiscale model to provide a two-way communicating path that is able to fit *in vitro* data from the nanomachine and *in situ* data from the intact muscle. In this way, the model can account for and identify the methodological reasons that limit the nanomachine performance when it fails to achieve the expected muscle performance. In perspective, the model and the nanomachine integrate to provide a new powerful tool for future applications in which the performance of the synthetic nanomachine powered by mutant and engineered myosins can be exploited to predict their outcome at the organ level.

References

Bagshaw CR & Reed GH (1977). The significance of the slow dissociation of divalent metal ions from myosin 'regulatory' light chains. *FEBS Lett* **81**, 386–390.

Bárány M (1967). ATPase activity of myosin correlated with speed of muscle shortening. *J Gen Physiol* **50**, 197–218.

Barclay CJ (2015). Energetics of contraction. *Compr Physiol* **5**, 961–995.

Barclay CJ, Woledge RC & Curtin NA (2010). Inferring cross-bridge properties from skeletal muscle energetics. *Prog Biophys Mol Biol* **102**, 53–71.

Baylor SM & Hollingworth S (2012). Intracellular calcium movements during excitation-contraction coupling in mammalian slow-twitch and fast-twitch muscle fibers. *J Gen Physiol* **139**, 261–272.

Bers DM, Patton CW & Nuccitelli R (2010). A practical guide to the preparation of Ca(2+) buffers. *Methods Cell Biol* **99**, 1–26.

Brandt PW, Reuben JP & Grundfest H (1972). Regulation of tension in the skinned crayfish muscle fiber. II. Role of calcium. *J Gen Physiol* **59**, 305–317.

Bremel RD & Weber A (1975). Calcium binding to rabbit skeletal myosin under physiological conditions. *Biochim Biophys Acta* **376**, 366–374.

Brunello E, Caremani M, Melli L, Linari M, Fernandez-Martinez M, Narayanan T, Irving M, Piazzesi G, Lombardi V & Reconditi M (2014). The contributions of filaments and cross-bridges to sarcomere compliance in skeletal muscle. *J Physiol* **592**, 3881–99.

Caputo C, Edman KA, Lou F & Sun YB (1994). Variation in myoplasmic Ca^{2+} concentration during contraction and relaxation studied by the indicator fluo-3 in frog muscle fibers. *J Physiol* **478**, 137–148.

Caremani M, Melli L, Dolfi M, Lombardi V & Linari M (2013). The working stroke of the myosin II motor in muscle is not tightly coupled to release of orthophosphate from its active site. *J Physiol* **591**, 5187–5205.

Craig R & Offer G (1976). Axial arrangement of crossbridges in thick filaments of vertebrate skeletal muscle. *J Mol Biol* **102**, 325–332.

Dantzig JA, Hibberd MG, Trentham DR & Goldman YE (1991). Cross-bridge kinetics in the presence of MgADP investigated by photolysis of caged ATP in rabbit psoas muscle fibres. *J Physiol* **432**, 639–680.

Dawson MJ, Gadian DG & Wilkie DR (1978). Muscular fatigue investigated by phosphorus nuclear magnetic resonance. *Nature* **274**, 861–866.

Elangovan R, Capitanio M, Melli L, Pavone FS, Lombardi V & Piazzesi G (2012). An integrated in vitro and in situ study of kinetics of myosin II from frog skeletal muscle. *J Physiol* **590**, 1227–1242.

Ferenczi MA, Homsher E, Trentham DR & Weeds AG (1978). Preparation and characterization of frog muscle myosin subfragment 1 and actin. *Biochem J* **171**, 155–163.

Ford LE, Huxley AF & Simmons RM (1977). Tension responses to sudden length change in stimulated frog muscle fibers near slack length. *J Physiol* **269**, 441–515.

Fromherz S & Szent-Gyorgyi AG (1995). Role of essential light chain EF hand domains in calcium binding and regulation of scallop myosin. *Proc Natl Acad Sci USA* **92**, 7652–7656.

Goldman YE, Hibberd MG & Trentham DR (1984). Relaxation of rabbit psoas muscle fibres from rigor by photochemical generation of adenosine-5′-triphosphate. *J Physiol* **354**, 577–604.

Hill AV (1938). The heat of shortening and the dynamic constants of muscle. *Proc R Soc Lond B* **126**, 136–195.

Huxley AF & Simmons RM (1971). Proposed mechanism of force generation in striated muscle. *Nature* **233**, 533–538.

Huxley AF (1957). Muscle structure and theories of contraction. *Prog Biophys Biophys Chem* **7**, 255–318.
Ishijima A, Kojima H, Higuchi H, Harada Y, Funatsu T & Yanagida T (1996). Multiple- and single-molecule analysis of the actomyosin motor by nanometer-piconewton manipulation with a microneedle: unitary steps and forces. *Biophys J* **70**, 383–400.
Kampourakis T & Irving M (2015). Phosphorylation of myosin regulatory light chain controls myosin head conformation in cardiac muscle. *J Mol Cell Cardiol* **85**, 199–206.
Kaya M & Higuchi H (2010). Nonlinear elasticity and an 8-nm working stroke of single myosin molecules in myofilaments. *Science* **329**, 686–689.
Kron SJ, Toyoshima YY, Uyeda TQ & Spudich JA (1991). Assays for actin sliding movement over myosin-coated surfaces. *Methods Enzymol* **196**, 399–416.
Kushmerick MJ & Davies RE (1969). The chemical energetics of muscle contraction. II. The chemistry, efficiency and power of maximally working sartorius muscles. Appendix. Free energy and enthalpy of ATP hydrolysis in the sarcoplasm. *Proc R Soc Lond B Biol Sci* **174**, 315–353.
Linari M & Woledge RC (1995). Comparison of energy output during ramp and staircase shortening in frog muscle fibers. *J Physiol* **487**, 699–710.
Linari M, Piazzesi G, Pertici I, Dantzig JA, Goldman YE & Lombardi V (2020). Straightening out the elasticity of myosin cross-bridges. *Biophys J* **118**, 994–1002.
Lombardi V, Piazzesi G & Linari M (1992). Rapid regeneration of the actin-myosin power stroke in contracting muscle. *Nature* **355**, 638–664.
Lymn RW & Taylor EW (1971). Mechanism of adenosine triphosphate hydrolysis by actomyosin. *Biochemistry* **10**, 4617–4624.
Nyitrai M & Geeves MA (2004). Adenosine diphosphate and strain sensitivity in myosin motors. *Philos Trans R Soc Lond B Biol Sci* **359**, 1867–1877.
Pardee JD & Spudich JA (1982). Purification of muscle actin. *Methods Enzymol* **85**, 164–181.
Pertici I, Bongini L, Melli L, Bianchi G, Salvi L, Falorsi G, Squarci C, Bozó T, Cojoc D, Kellermayer MSZ, Lombardi V & Bianco P (2018). A myosin II nanomachine mimicking the striated muscle. *Nat Commun* **9**, 3532.
Pertici I, Bianchi G, Bongini L, Lombardi V & Bianco P (2020). A myosin II-based nanomachine devised for the study of Ca^{2+}-dependent mechanisms of muscle regulation. *Int J Mol Sci* **21**, 7372.
Piazzesi G & Lombardi V (1995). A cross-bridge model that is able to explain mechanical and energetic properties of shortening muscle. *Biophys J* **68**, 1966–1979.
Piazzesi G, Reconditi M, Koubassova N, Decostre V, Linari M, Lucii L & Lombardi V (2003). Temperature dependence of the force-generating process in single fibers from frog skeletal muscle. *J Physiol* **549**, 93–106.
Piazzesi G, Reconditi M, Linari M, Lucii L, Bianco P, Brunello E, Decostre V, Stewart A, Gore DB, Irving TC, Irving M & Lombardi V (2007). Skeletal muscle performance determined by modulation of number of myosin motors rather than motor force or stroke size. *Cell* **131**, 784–795.
Rayment I, Holden HM, Whittaker M., Yohn CB, Lorenz M, Holmes KC & Milligan RA (1993). Structure of the actin-myosin complex and its implications for muscle contraction. *Science* **261**, 58–65.
Reconditi M, Brunello E, Fusi L, Linari M, Martinez MF, Lombardi V, Irving M & Piazzesi G (2014). Sarcomere-length dependence of myosin filament structure in skeletal muscle fibres of the frog. *J Physiol* **592**, 1119–1137.
Smith DA & Geeves MA (1995). Strain-dependent cross-bridge cycle for muscle. *Biophys J* **69**, 524–537.
Suzuki N, Miyata H, Ishiwata S & Kinosita K (1996). Preparation of bead-tailed actin filaments: estimation of the torque produced by the sliding force in an in vitro motility assay. *Biophys J* **70**, 401–408.
Szczesna D, Ghosh D, Li Q, Gomes AV, Guzman G, Arana C, Zhi G, Stull JT & Potter JD (2001). Familial hypertrophic cardiomyopathy mutations in the regulatory light chains of myosin affect their structure, Ca^{2+} binding, and phosphorylation. *J Biol Chem* **276**, 7086–7092.
Szczesna D, Zhao J, Jones M, Zhi G, Stull J & Potter JD (2002). Phosphorylation of the regulatory light chains of myosin affects Ca^{2+} sensitivity of skeletal muscle contraction. *J Appl Physiol* **92**, 1661–1670.
Szent-Gyorgyi AG (1975). Calcium regulation of muscle contraction. *Biophys J* **15**, 707–723.
Tanaka H, Ishijima A, Honda M, Saito K & Yanagida T (1998). Orientation dependence of displacements by a single one-headed myosin relative to the actin filament. *Biophys J* **75**, 1886–1894.
Toyoshima YY, Kron SJ, McNally EM, Niebling KR, Toyoshima C & Spudich JA (1987). Myosin subfragment-1 is sufficient to move actin filaments in vitro. *Nature* **328**, 536–539.
Tyska MJ & Warshaw DM (2002). The myosin power stroke. *Cell Motil Cytoskeleton* **51**, 1–15.
Uyeda TQ, Kron SJ & Spudich JA (1990). Myosin step size. Estimation from slow sliding movement of actin over low densities of heavy meromyosin. *J Mol Biol* **214**, 699–710.
Weeds AG & Taylor RS (1975). Separation of subfragment-1 isoenzymes from rabbit skeletal muscle myosin. *Nature* **257**, 54–56.
Woledge RC, Curtin NA & Homsher E (1985). *Energetic aspects of muscle contraction*. Academic Press, London.

Additional information

Data availability statement

The data that support the findings of this study are available from the corresponding author upon reasonable request.

Competing interests

The authors declare that they have no competing interests.

Author contributions

VL and PB conceived the study. IP, VL and PB designed the experiment and implemented the procedure. IP and PB executed the nanomachine experiments and analysed the data. IP and MHT performed the ATPase measurements. LB, VL, PB and GB implemented the model simulation. DC performed etching of myosin supports. VL and DJM contributed to drafting or critical revision of the article.

Funding

This work was supported by Istituto Italiano di Tecnologia, SEED-2009 (Italy), Ente Cassa di Risparmio di Firenze Project 2010.1402, 2015.0902 and 2016.1108 (Italy). DJM received grant support from the Deutsche Forschungsgemeinschaft (MA1081/22-1).

We thank Gabriella Piazzesi for reading and commenting the manuscript.

Keywords

frog myosin, myosin-based nanomachine, myosin ensemble mechanics

Supporting information

Additional supporting information may be found online in the Supporting Information section at the end of the article.

Statistical Summary Document